High-Brightness VCSEL Arrays With Inter-Mesa Waveguides for the Enhancement of Efficiency and High-Speed Data Transmission

Jie-Chen Shih ⓘ, Zuhaib Khan, Yung-Hao Chang, and Jin-Wei Shi ⓘ, *Senior Member, IEEE*

Abstract—**A novel VCSEL array for high-efficiency, high-speed, and high-brightness performance is demonstrated. In contrast to the traditional VCSEL arrays, which have several independent VCSEL cavities in parallel, the novel array structure has additional passive optical waveguides connecting each cavity. In addition, Zn-diffusion and oxide-relief structures are adopted for each single element of the array to obtain the high-brightness (single-mode; SM) output and relax the RC-limited bandwidth. Comparison is made to the traditional reference array. Although the values of the oxide-relief apertures are close to each other, the novel demonstrated arrays exhibit a higher wall plug efficiency, larger maximum output power, and better eye-opening for high-speed data transmission, when both of their output optical spectra are quasi-(SM) with close narrow divergence angle values (FWHM: ∼6°). The superior performance of the demonstrated array for (quasi-) SM operation can be attributed to the dilution of the photon density in the SM output pattern from each VCSEL unit through the connections of passive waveguide. Furthermore, it also enhances the coherence between the neighboring VCSEL emitters, minimizing their interference noise which occurs under large signal modulation. This novel 940 nm VCSEL array has good potential to serve as a light source in free-space optical communication.**

Index Terms—**Semiconductor lasers, semiconductor laser arrays, vertical-cavity surface emitting lasers (VCSEL).**

I. INTRODUCTION

RECENTLY, high-speed and high-brightness vertical-cavity surface-emitting laser (VCSEL) arrays, which can serve as the light sources in advanced time-of-flight (ToF) lidar sensing and free space optical (FSO) communications systems [1]–[4], have attracted a lot of attention. An FSO SpaceComm network for linking between different micro or nanosatellites has been successfully established [5]–[7]. For such systems, a linking distance of up to hundreds of kilometers with a data transmission rate of around 20 Mbit/sec is necessary [5], [6],

and a high-power (output of hundreds of mW under CW operation), high-brightness, high-speed light source plays a crucial role. The output of high-brightness light sources with narrow divergence angles can minimize the diffraction loss resulting from optical beam propagation and enhance the optical power received by a high-speed receiver (sensor) with a limited active area. Compared with the edge-emitting lasers (EELs) for FSO aerospace applications, VCSELs usually show better radiation resistance [8], [9]. However, the commercially available high-speed VCSELs usually have a wide divergence angle ($1/e^2$: ∼25°) with small output power performance. Narrowing the divergence angle of the far-field patterns (FFPs) in high-power and high-speed VCSEL arrays is an effective way to attain the desired output power level and brightness needed to meet the demands of the afore-mentioned applications [10]–[12]. The monolithic integration of an intra-cavity collimating lens into the multi-mode (MM) VCSEL array has allowed the development of 940 nm wavelength VCSEL arrays with high-power and high-brightness output beams for lidar and 3-D sensing applications [12]. However, the pitch size of a VCSEL unit in the array is limited by the lens integrated into the substrate side. One of the most effective ways to significantly narrow the far-field divergence angle and enhance the brightness is to build a VCSEL array of single-mode VCSEL units [10], [11]. Several VCSEL structural designs for attaining high SM power have been reported, including surface-relief [13], Zn-diffusion [14], photonic crystal [15], and anti-guide (leaky) cavity structures [16]. However, the spatial hole burning (SHB) effect, which originates from the high optical power density in the high brightness output beam of these high-power SM VCSELs, usually leads to a serious low-frequency roll-off in their electrical-optical (E-O) frequency responses and degradation in the quality of the eye-patterns for high-speed data transmission [17], [18]. Furthermore, degradation in the modulation speed of a parallel VCSEL array as compared to that of a single unit is usually observed, due to the increase in the parasitic capacitance [1], [3], [4]. In this study, we demonstrate a novel 940 nm VCSEL array structure for high-brightness, high-efficiency, and high-speed performance fabricated using Zn-diffusion and oxide-relief techniques [3], [19], [20], which can greatly relax the RC-limited bandwidth of the array and enhance its brightness performance. In contrast to the traditional VCSEL arrays, which have several independent single VCSEL cavities arranged in parallel, the
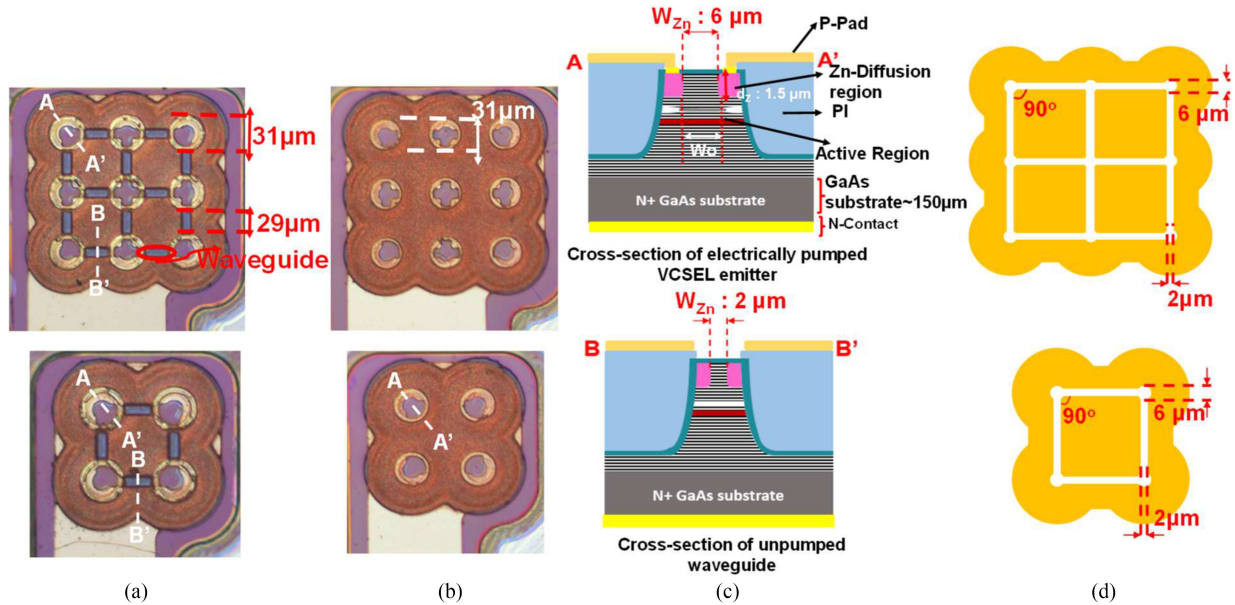
Fig. 1. Top view of the demonstrated 2 × 2 and 3 × 3 VCSEL (a) array A and (b) array B, respectively. (c) Conceptual cross-sectional view of the passive waveguides and active mesas in array A. This figure is not drawn according to scale for clarity. (d) Layout of the Zn-diffusion patterns in the array. The yellow areas represent the regions with Zn-diffusion patterns.

new design demonstrated here has additional passive optical waveguides connecting each VCSEL cavity. Compared to the traditional reference array with close values of Zn-diffusion and oxide-relief apertures for SM operation, the demonstrated array shows a significant improvement in the wall plug efficiency (WPE), eliminating the low-frequency roll-off in the E-O responses, which greatly enhances the quality of the eye-patterns for high-speed data transmission, while maintaining the same narrow divergence angle (full-width half-maximum: ∼6°). These superior performance characteristics of the demonstrated array can be attributed to the fact that the high photon density in the SM output pattern from each VCSEL unit is diluted through the connected passive waveguides between the different apertures. The reduction in photon density for SM operation can thus release the SHB effect. Furthermore, the waveguide connection also enhances the coherence between the neighboring VCSEL emitters, minimizing the interference noise and cross-talk which occurs between them under large signal modulation. In modern nanosatellites, two kinds of laser sources, at wavelengths of around 970 and 1550 nm, are used for beacon and data communication, respectively [5]. The demonstrated high-speed and high-brightness 940 nm VCSEL array has the potential to simultaneously satisfy the requirements for both of these applications (beacon and communication) while greatly simplifying the design and reducing the size of the optics system in the newly deployed FSO network.

II. DEVICE STRUCTURE DESIGN AND FABRICATION

Figs. 1(a) and (b) show top-views of the demonstrated 2 × 2 and 3 × 3 arrays. Two kinds of structures for each size of array were fabricated for comparison: one with optical waveguides to connect each VCSEL unit (array A) The other is the traditional array structure (array B) having the same mesa sizes but without the waveguides. The waveguide length and width in array A is 29 and 6 μm, respectively. Three different oxide aperture (W_o) diameters as 9, 12, and 15 μm in both array (A and B) structures are studied. The corresponding mesa diameter for each W_o (9, 12, and 15 μm) is adjusted to 28, 31, and 34 μm, respectively, to meet the desired values of W_o. For the case of W_o as 12 μm, the mask defined mesa diameter is 35 μm, but it becomes 31 μm after the wet etching process with a depth of 4 μm and 2 μm lateral etching. The optical waveguides which connect the different active VCSEL units are specified in these two photos. Fig. 1(c) shows conceptual cross-sectional views of the active light-emitting mesa and passive waveguides in array A. As can be seen, the Zn-diffusion and oxide-relief processes have been performed on each unit's active VCSEL in order to manipulate the optical transverse modes and relax the RC-limited bandwidth of the array [3]. The passive waveguides between the different active mesas are composed of the same epi-layer structure as the VCSEL cavity [21]. The p- and n-type distributed Bragg reflectors (DBRs) serve as the waveguide claddings and the active layers serve as the waveguide core. The passive waveguide regions are sealed by a dielectric film to isolate them from the external current injection. Zn-diffusion apertures are also applied to the passive waveguide regions in order to enhance the optical confinement in the transverse direction. The detailed geometry and size of the diffusion depths and widths are specified in Fig. 1(c) and Fig. 2(a). In our cavity design, the photoluminescence (PL) peak wavelength of our MQW active region is at around 924 nm at RT. Based on the measured Bragg wavelength (∼937 nm) in our VCSEL cavity, the corresponding cavity-to-PL detuning wavelength is around 13 nm. Such a design can not only improve the high-temperature performance of the VCSEL [22], [23] but also ensure that our
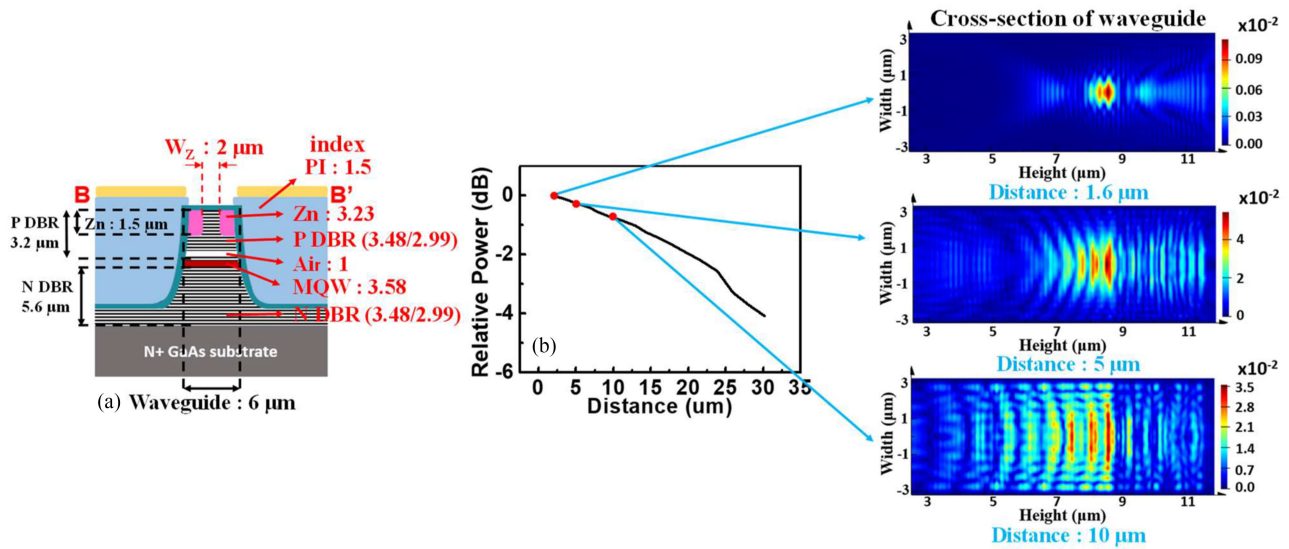
Fig. 2. (a) Conceptual cross-sectional view of the passive waveguides used for optical simulation. The refractive indexes of each layer are specified. (b) Simulated total optical power versus propagation distance in our waveguide. The insets show the simulated cross-sectional optical mode field patterns at different waveguide locations. PI: polymethylglutarimide.

passive waveguide will be transparent for the propagation of lasing light with a central wavelength at around 940 nm. Optical confinement in the direction perpendicular to the wafer surface of the passive waveguide is achieved by the index contrast between the III-V active multiple quantum wells (MQWs) and the thin ($\sim$28 nm) air layer, which is realized by the oxide-relief process, as discussed above. Details about the design and simulation of our passive waveguide are illustrated in Fig. 2. Fig. 1(d) shows the detailed layout of the Zn-diffusion patterns in this array. The yellow region represents the Zn-diffusion area. In order to enhance the mutual coupling between different VCSEL unit through optical waveguides in array A, the lossy Zn-diffusion regions in the junction between the waveguides and the active mesas have been removed, which changes the Zn-diffusion apertures from ring- to fan-shaped. Fig. 2(a) shows a conceptual cross-sectional view of the passive waveguide used in the optical simulation. The refractive index of each DBR layer is specified in this figure. The effective index in the active MQWs and Zn-diffusion (disordering) regions is determined by the weighting of the thickness and index of each layer. Fig. 2(b) shows the simulated total optical power inside the waveguide versus the propagation distance and the optical mode field distribution at different positions on the waveguide cross-section. Here, we adopted commercially available software[1] to simulate the optical waveguide structure. As can be seen, a highly multi-mode and moderate insertion loss (-4 dB) within the propagation distance (30 μm) between different active mesas can be sustained. This result indicates that the demonstrated waveguide structure can effectively link and increase the coherence between different light emission units in the array.

There are three key parameters for the active mesa: W_Z, W_O, and d, which determine the mode characteristics of the single device. Here, W_Z and W_O represent the diameter of the Zn-diffusion aperture and oxide-confined aperture, respectively; d is the Zn-diffusion depth. The addition of Zn-diffusion apertures in the top p-type DBR layers of our VCSEL will induce extra loss in the peripheral region of the optical aperture. Higher order mode lasing can thus be suppressed in the Zn-diffused DBR region due to free-carrier absorption and reflectivity reduction caused by disordering [14], [17]. The disordering of the DBR layers allows us not only to manipulate the number of optical transverse modes inside the VCSEL cavity, as discussed elsewhere, but can also reduce the differential resistance of the VCSEL [3]. By properly optimizing the relative sizes of these three parameters to allow significant Zn-diffusion induced internal loss (α_i) in the current-confined (gain) region, the device is able to demonstrate high single-mode (SM) performance under the full range of bias currents [10], [14], [17]. The values of W_Z and d for all VCSEL units in arrays A and B, are fixed at 6.0 and 1.5 μm. Different values of W_o are adopted to study the influence of the output optical spectra of the VCSEL units on the static and dynamic performance of both arrays (A and B). The epi-layer structure which is grown in a molecular beam epitaxy (MBE) chamber[2] is composed of six compressive strained $In_{0.13}Ga_{0.87}As/Al_{0.08}Ga_{0.92}As$ MQWs sandwiched between 38-paired n-type and 20-paired p-type $Al_{0.93}Ga_{0.07}As/Al_{0.06}Ga_{0.94}As$ (50.9/50.2 nm thickness) Distributed-Bragg-Reflector (DBR) layers with a single $Al_{0.98}Ga_{0.02}As$ layer (28 nm thick) for oxidation. The fabrication of the array starts with the Zn-diffusion process. A high-quality Si_3N_4 film is necessary to serve as the mask for the high-temperature diffusion
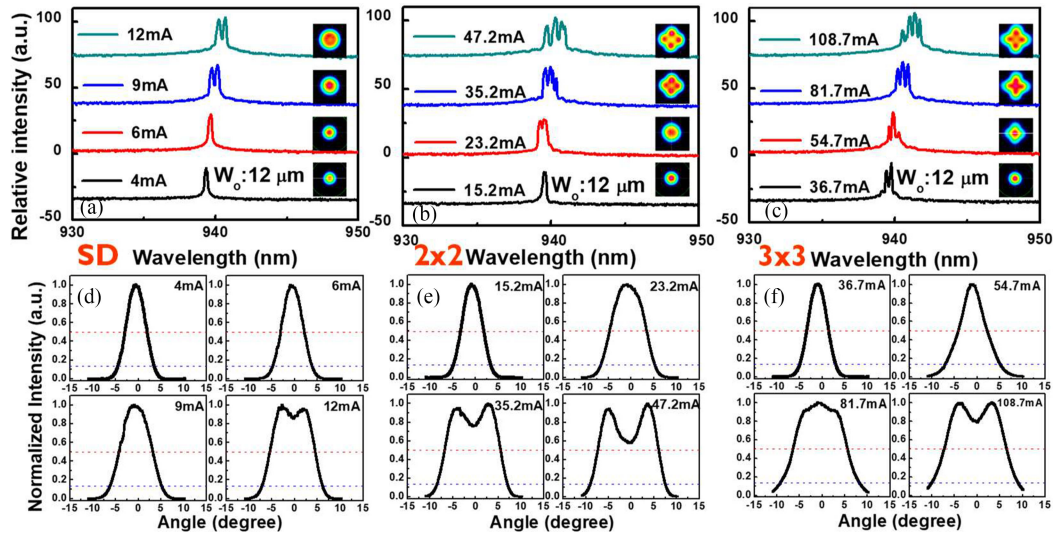
Fig. 3.   Measured bias dependent optical spectra and 2-D FFPs of array A ($W_z/W_o/d$ = 6.0/12/1.5 μm) for a (a) single device (SD), (b) 2 × 2 array, and (c) 3 × 3 array. The corresponding 1-D bias dependent FFPs for the (d) single device (SD), (e) 2 × 2 array, and (f) 3 × 3 array.

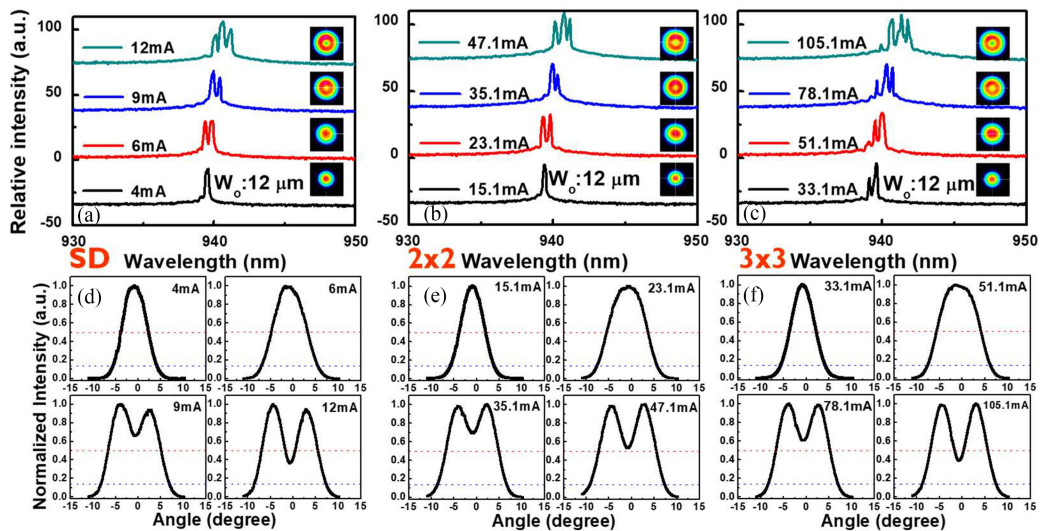
Fig. 4.   Measured bias dependent optical spectra and 2-D FFPs of array B ($W_z/W_o/d$ = 6.0/12/1.5 μm) for a (a) single device (SD), (b) 2 × 2 array, and (c) 3 × 3 array. The corresponding 1-D bias dependent FFPs for the (d) single device (SD), (e) 2 × 2 array, and (f) 3 × 3 array.

process. The mask defined diameter of the optical aperture (without Zn-diffusion) is around 8 μm. Considering lateral Zn-diffusion, the final W_z is around 6.0 μm after the completion of the Zn-diffusion process and ∼1.5 μm in depth (d). After the diffusion process, the mesa and waveguide etching process is performed. Although the shape of the mesa is not circular after wet etching, a circular current-confined area can still be obtained after the wet oxidation process. In order to have different sizes of W_o, 3 different diameters of mesas are used and this results in a W_o of 9, 12, and 15 μm. After p-type contact metallization (Ti/Au;50/200 nm), the device is passivated by the addition of a SiO2 layer (∼150 nm) and an ∼3 μm thick polymethylglutarim-ide (PMGI) layer is then deposited for planarization. Finally, an ∼2 μm thick Ti/Au layer is evaporated onto the chip for on-wafer probing.

III. MEASUREMENT RESULTS

Note that for each device structure discussed in the following sections of this paper, we conducted measurements of at least 3 devices for each structure, all showing very similar performance. The L-I-V curves of all our studied devices are shown in Figs. 7 and 8. Here, we would first like to discuss the bias dependent output optical spectra and 2-D/1-D far-field patterns for arrays A and B (with different numbers of elements), as shown in Figs. 3 and 4, respectively. The oxide-relief aperture (W_o) is fixed at 12 μm. Figs. 5 and 6 show similar measurement results but for the cases were W_o is increased from 12 to 15 μm. We can clearly see that the bias dependent behaviors of the output optical spectra of both array structures (A and B) are pretty close and the optical spectra switches from MM to quasi-SM
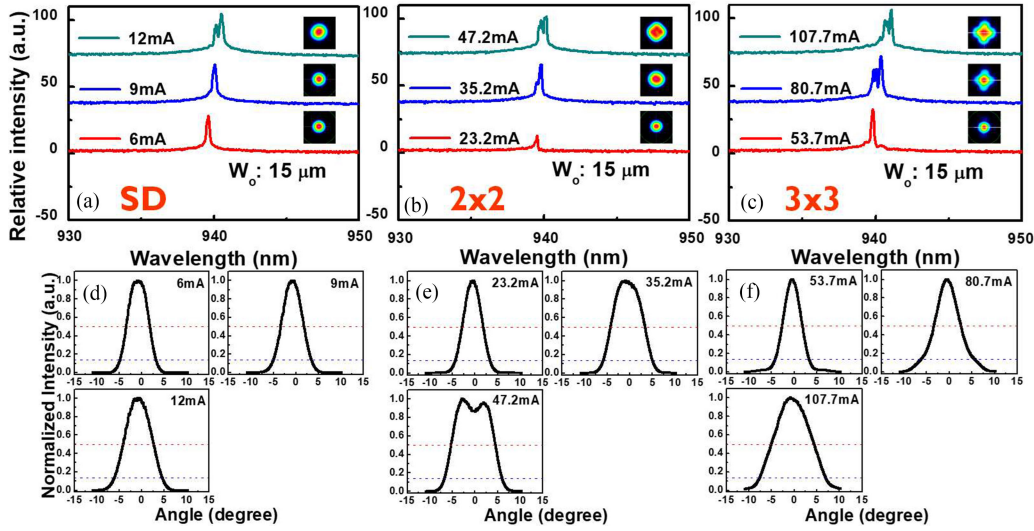
Fig. 5. Measured bias dependent optical spectra and 2-D FFPs of array A ($W_z/W_o/d = 6.0/15/1.5~\mu m$) for a (a) single device (SD), (b) 2×2 array, and (c) 3×3 array. The corresponding 1-D bias dependent FFPs for the (d) single device (SD), (e) 2×2 array, and (f) 3×3 array.
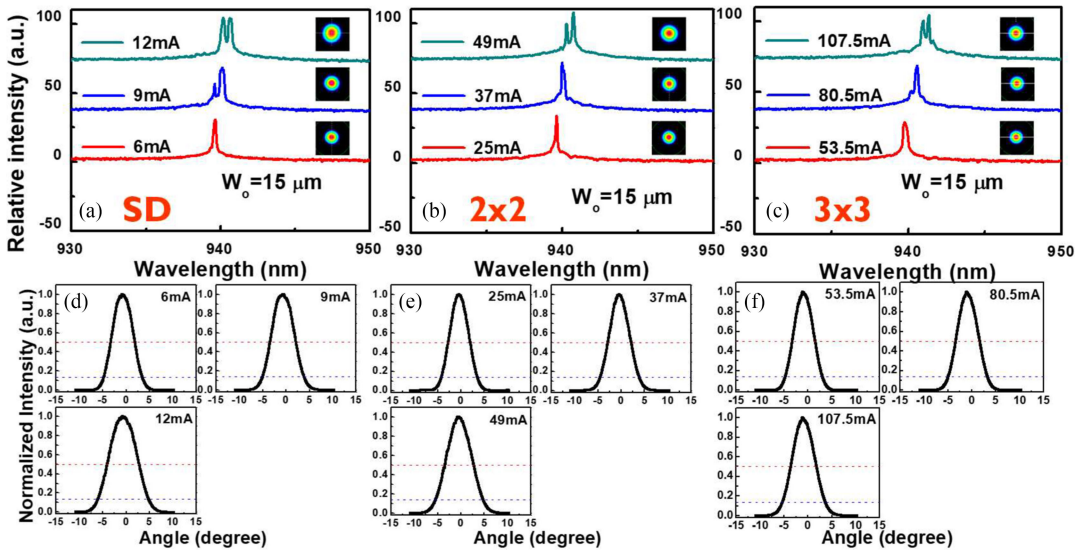

Fig. 6. Measured bias dependent optical spectra and 2-D FFPs of array B ($W_z/W_o/d = 6.0/15/1.5~\mu m$) for a (a) single device (SD), (b) 2×2 array, and (c) 3×3 array. The corresponding 1-D bias dependent FFPs for the (d) single device (SD), (e) 2×2 array, and (f) 3×3 array.

when W_o increases from 12 to 15 μm, due to the increase in the Zn-diffused intra-cavity loss, as previously discussed [10], [17]. As can be seen in Figs. 4 and 6, the FFP of array B, with different numbers of elements (2×2 and 3×3), is exactly the same as that of the reference single device. Under MM operation (W_o: 12 μm), the 2-D FFP becomes donut-like with an indentation in the center ($\sim 40\%$) but for SM operation, the FFP becomes Gaussian-like with a narrow divergence angle (full-width half maximum (FWHM): $\sim 6°$). These results are the same as those quite commonly reported for the MM [12] and SM VCSEL arrays [10] and imply that, without inter-mesa waveguide connections, each VCSEL unit in the array lases almost independently [10]. On the other hand, compared with array B, there is a dramatic change in the FFPs of array A,

as shown in Figs. 3 and 5. This suggests that the inter-mesas waveguides not only dilute the photon density inside a single VCSEL cavity but also lock the phase between neighboring VC-SEL emitters. We can clearly see that the 2-D FFP of MM array A (W_o:12 μm) under high bias current (47 mA for 2×2) exhibits 4 distinct peaks in space, as is usually observed in the reported phase-locked VCSEL array under out-of-phase lasing operation [23], [24]. However, in the quasi-SM array A (W_o:15 μm), single-spot FFPs, which have divergence angles close to those of quasi-SM array B (W_o:15 μm), can still be sustained under the full range of bias currents. Tables I to IV summarize the FFPs obtained for multi-mode (MM) (W_o: 9 μm) and (quasi-) SM arrays A and B (W_o:15 μm), respectively, under different bias currents. The corresponding output power and divergence angles
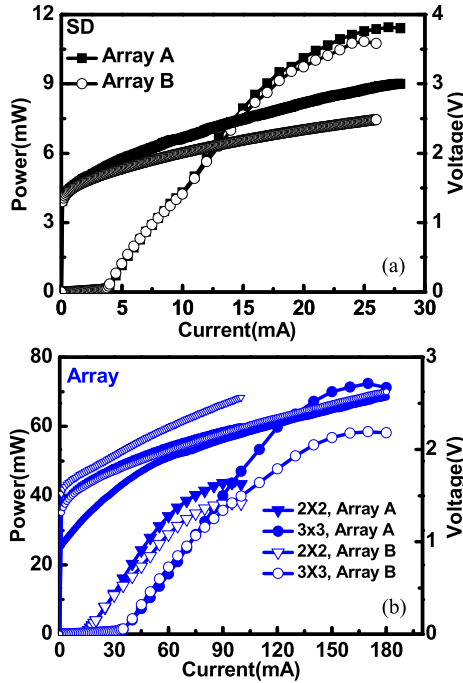
Fig. 7. Measured L-I-V curves for a (a) single device (SD), (b) arrays A and B having (2×2) and (3×3) emitters, respectively (Wz/Wo/d = 6.0/15/1.5 μm).
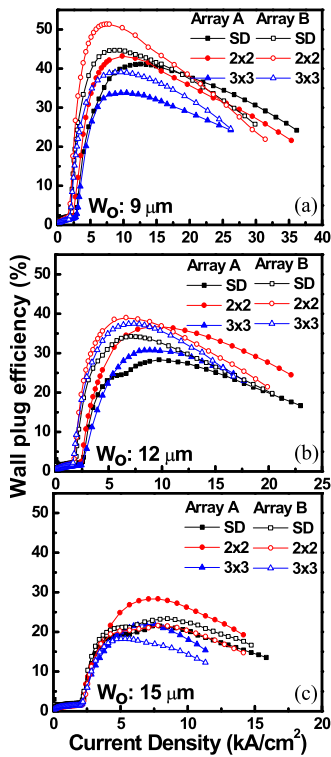

Fig. 8. Measured WPEs vs. driving current density of arrays A and B (Wz/d = 6.0/1.5 μm) with different numbers of emitters (SD, 2 × 2, and 3 × 3) and different oxide aperture sizes of (a) 9 μm, (b) 12 μm, and (c) 15 μm.

TABLE I
SUMMARIZED BIAS DEPENDENT FFPS OF ARRAY A WITH DIFFERENT
NUMBERS OF EMITTERS (W$_Z$/W$_O$/D = 6.0/9/1.5 μm)

TABLE II
SUMMARIZED BIAS DEPENDENT FFPS OF ARRAY B WITH DIFFERENT
NUMBERS OF EMITTERS (W$_Z$/W$_O$/D = 6.0/9/1.5 μm)

TABLE III
SUMMARIZED BIAS DEPENDENT FFPS OF ARRAY A WITH DIFFERENT
NUMBERS OF EMITTERS (W$_Z$/W$_O$/D = 6.0/15/1.5 μm)

(FWHM) obtained under each bias current are given in these four tables. The total (black) and averaged I$_{th}$ (yellow) values for the arrays and for each single device, respectively are also specified. In Tables I and II we can clearly see that the average I$_{th}$ values are larger for array A than array B. This also holds true for single reference devices and for both structures, which implies that the leakage current into the passive waveguide is not an issue for a larger I$_{th}$. The variation in I$_{th}$ performance of the single reference devices in array A and array B may be attributed to variations in the process and uniformity issues in 6-inch VCSEL wafers in the different samples. Here, in order to make a fair comparison between a single reference device and an array, we place the single device as close as possible to the arrays. Array A and B share the same mesa structure for their single reference VCSEL [19], [20] and are fabricated from the same VCSEL wafer (6-inch) but from different samples, so it is difficult to ensure that two different samples will have

TABLE IV
SUMMARIZED BIAS DEPENDENT FFPS OF ARRAY B WITH DIFFERENT
NUMBERS OF EMITTERS ($W_Z/W_O/D = 6.0/15/1.5$ μm)

TABLE V
SUMMARIZED SLOPE EFFICIENCY AND MAXIMUM OUTPUT POWER FOR
ARRAYS A AND B ($W_Z/W_O/D = 6.0/15/1.5$ μm)

Type of Array	Type of device	Slope Efficiency ($^{dP}/_{dI}$)	Maximum Output power(mW)
Array A	SD	0.77@12mA	11.5
	2X2 Array	0.78@45mA	44
	3X3 Array	0.77@85mA	72
Array B	SD	0.73@12mA	10.8
	2X2 Array	0.52@40mA	38
	3x3 Array	0.48@80mA	58

exactly the same W_o. Nevertheless, as shown in Tables I to IV, these single devices (SD) provide a good reference in terms of the I_{th} for their corresponding array structure. On the other hand, when we increase the W_o to 15 μm for SM performance (see Tables III and IV), the difference in I_{th} between array A and B becomes smaller. This can be attributed to the fact that, for SM operation, the Zn-diffusion induced intra-cavity loss gradually becomes the domiant factor of I_{th}. In the array A structure with waveguides, the cavity loss is less, due to that there being no Zn-diffused region in the junction between the waveguide and the mesa. Moreover, as can be seen in Tables III and IV, for a 3 × 3 array under a moderate bias current (80 mA), a higher output power (33 vs. 31 mW) is obtained for the array A structure than for array B, with the same divergence angle (FWHM: ∼6°). Under such operational conditions, array A exhibits a significant improvement in large-signal modulation, which will be discussed later; see Fig. 13. Figs. 7(a) and (b) show the measured L-I-V curves for the single device (W_o:15 μm) and arrays A and B, having oxide aperture values which are close to each other and with 2 × 2 and 3 × 3 emitters, measured under room temperature (RT) operation. Table V shows a summary of the corresponding slope efficiency and maximum output power. As can be seen, in array A, with waveguide connections between the different VCSEL units, the measured I_{th} is linearly proportional to the number of VCSEL units. This result also suggest that the injected current, which spreads from the active mesa to the passive waveguide region, is negligible. In addition, we can clearly see that we can obtain a significantly higher output power (slope efficiency) with array A than array B due to the additional passive waveguides inside the array. It appears that

the nominal maximum output power per emitter of the 3 × 3 array A drops to 2/3 of the value of a single emitter VCSEL. For array B, it drops even more, to about ∼55% when going from a single emitter to a 3 × 3 array. On the other hand, for the power values specified in Tables I and II, for MM arrays A and B, the degradation in output power per unit device is as small as ∼89%. Such a result clearly indicates that the SM induced SHB effect seriously limts the static perfromancess of our SM VCSEL array but it can be minimized by adapting the demonstrated array A structure. Figs. 8(a) to (c) show the extracted wall plug efficiencies (WPEs) versus driving current densities for arrays A and B obtained with three different oxide apertures (W_o) of 9, 12, and 15 μm, respectively. As discussed above, when we gradually increase the W_o, the output optical spectra will shift from MM to SM due to the increase of Zn-diffused intra-cavity loss. Fig. 8(a) shows the measurements for the MM VCSEL array (W_o: 9 μm). It can be seen that the array B structure exhibits a maximum WPE of around 50% (for the 2 × 2 array under a driving current of 7 kA/cm^2), which is superior to that of array A (50 vs. 40%). This can be attributed to the slight smaller W_o and I_{th} values, as specified in Tables I and II, for array B than for array A. Such a discrepancy is due to the problem of reproducibility for the wet oxidation process in these two samples (A and B), as noted above. Nevertheless, when the W_o increases for SM operation with high brightness output, the array A structure exhibits better WPE performance than that of array B, as can be seen in Fig. 8(c) (W_o: 15 μm). Under a driving current density of around 7 kA/cm^2, we obtain a larger WPE for array A with 2 × 2 elements and (quasi-) SM performance (29 vs. 21%) than that of reference array B. These FFP and L-I-V measurement results indicate that when the VCSEL array output varies from MM to SM, both the increase in the Zn-diffused intra-cavity loss and SHB effect, which is due to the high photon density in the single-spot optical mode field [17], [18], will lead to degradation in the WPE performance of the VCSEL array, becoming the major factor limiting its perfor-mances The proposed inter-mesa waveguide structures in array A can effectively dilute the photon density, minimizing the SHB effect, leading to an enhancement of the WPE, and sustaining of the single-spot FFP with a narrow divergence angle (high brightness).The high-speed electrical-to-optical (E-O) perfor-mance of the fabricated arrays was measured by a lightwave component analyzer (LCA), composed of a network analyzer (Anritsu 37397C) and a calibrated photoreceiver module (VI Systems: D50-1300 M)[3], which could cover an optical window from wavelengths of 850 to 1310 nm. The measured O-E -3dB bandwidths for this photoreceiver module at wavelengths of 850 and 1310 nm are around 27 and 24 GHz, respectively. Here, the measured optical-to-electrical (O-E) frequency responses at 850 nm are selected for calibration during the de-embedding pro-cess for 940 nm VCSEL E-O measurement. This should avoid overestimatation of the E-O bandwidth in our device. During measurement, a multi-mode fiber (MMF; OM3) with a ball lens tip is used to collect the light output from one of the single emit-ters in the array. The output of the MMF is then connected with

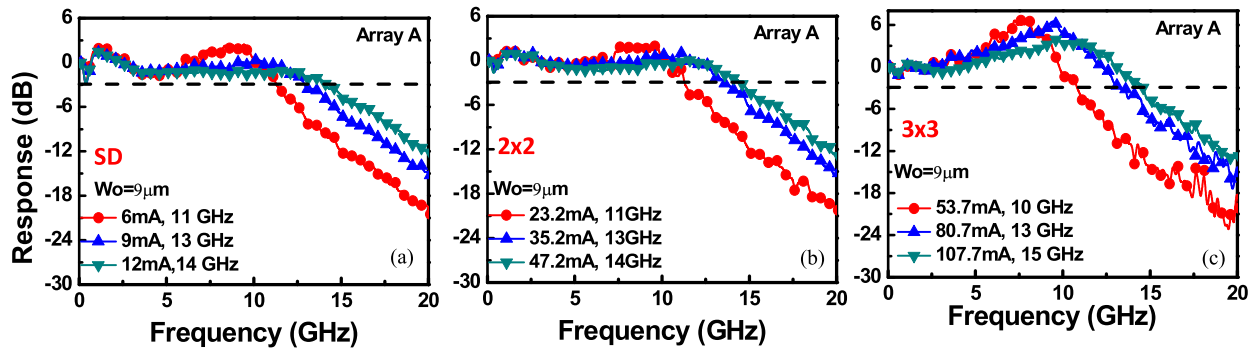[3]VI Systems GmbH, Hardenbergstrasse 7, 10623 Berlin, Germany.

Fig. 9. Measured bias dependent E-O responses of array A with (a) SD, (b) 2 × 2, and (c) 3 × 3 number of emitters (Wz/Wo/d = 6.0/9/1.5 μm).

Fig. 10. Measured bias dependent E-O responses of array B with (a) SD, (b) 2 × 2, and (c) 3 × 3 number of emitters (Wz/Wo/d = 6.0/9/1.5 μm).

Fig. 11. Measured bias dependent E-O responses of array A with (a) SD, (b) 2 × 2, and (c) 3 × 3 number of emitters (Wz/Wo/d = 6.0/15/1.5 μm).
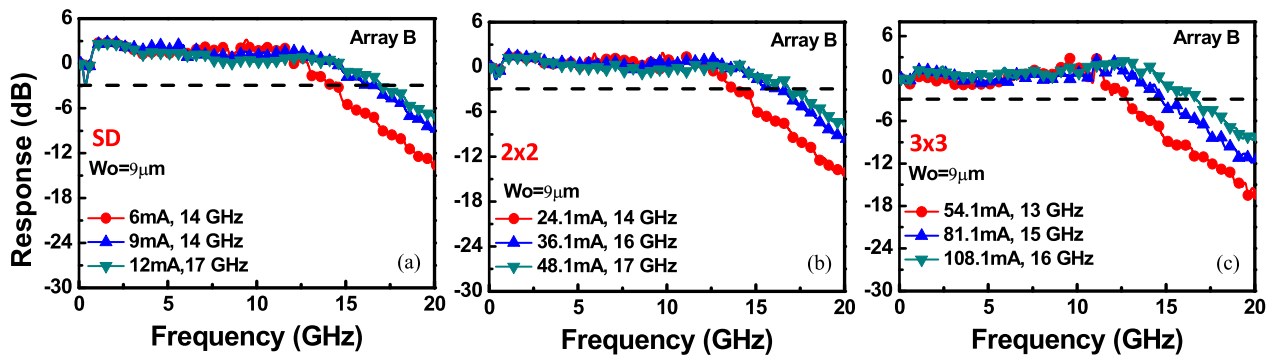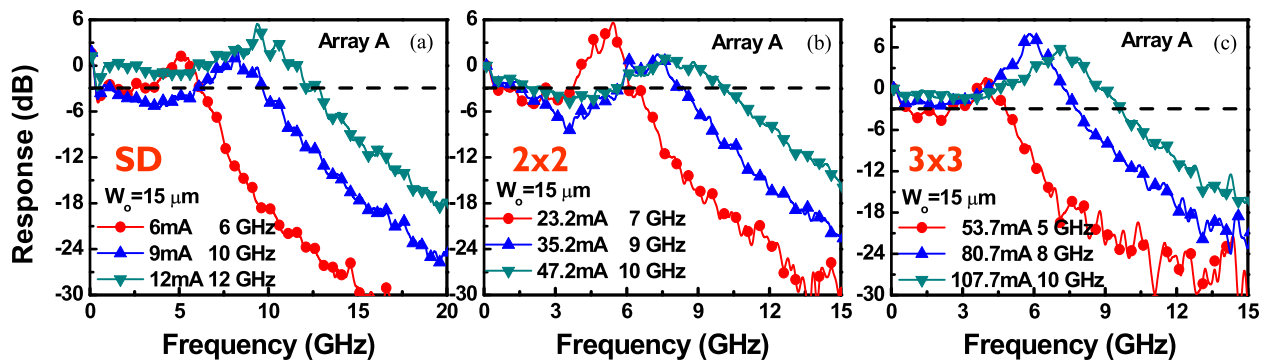
the photo-receiver module (D50-1300 M) as above-discussion. Figs. 9 to 12 show the measured bias dependent E-O frequency responses of multi-mode (W_o: 9 μm) and quasi-SM arrays A and B (W_o: 15 μm), respectively, with different numbers of emitters. Thanks to the Zn-diffusion and oxide-relief processes, which can effectively release the RC-limited bandwidth of the VCSELs [3], [19], [20], the measured maximum 3-dB E-O bandwidths of the single reference VCSEL are pretty close to those of arrays A and B (2 × 2 and 3 × 3 number of elements) for both the cases of devices with MM and SM performance. This result indicates that the external RC-limited bandwidth is not an issue in the net speed performance of our demonstrated array and the dominant

speed limiting factor should be the device heating and SHB effect in SM devices as discussed above.

For details about device modeling the interested reader can refer to our previous work [3]. In contrast to the measured E-O responses of VCSELs with MM performance (Figs. 9 and 10), there is an additional low-frequency roll-off (~6 dB) induced by the SHB effect [17], [18] in the measured E-O traces of SM arrays A and B (Figs. 11 and 12). This leads to degradation in the quality of the eye-pattern during high-speed data transmission [17], [18], as will be discussed later. The pronounced SHB effect in SM one occurs because it usually has a more concentrated far-field distribution. This leads to the hole recombination rate
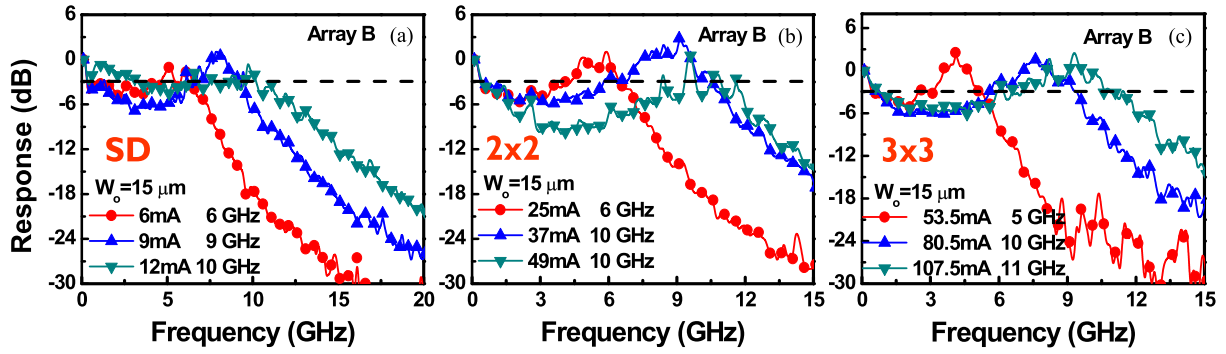
Fig. 12.   Measured bias dependent E-O responses of array B with (a) SD, (b) 2×2, and (c) 3×3 number of emitters ($W_z/W_o/d = 6.0/15/1.5$ μm).

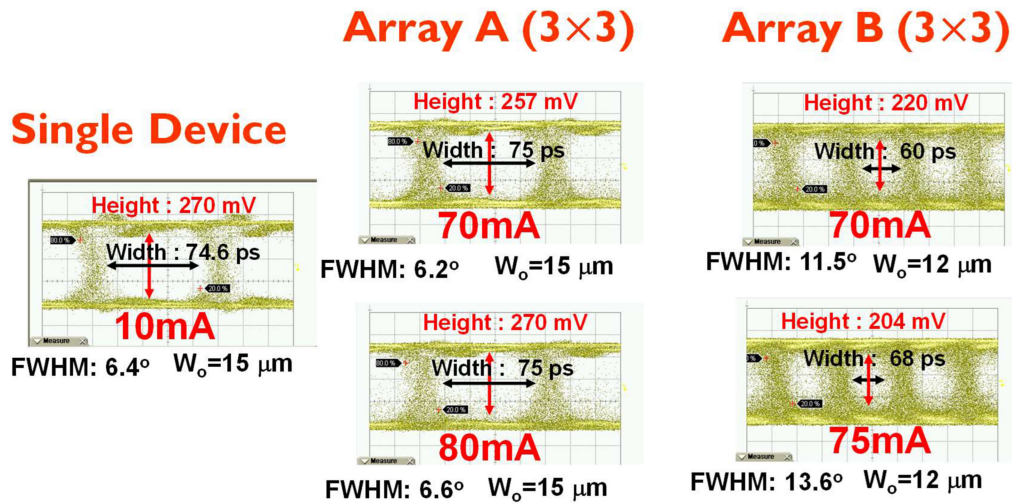Fig. 13.   Measured 10 Gbit/sec eye patterns of SD ($W_z/W_o/d = 6.0/15/1.5$ μm), array A ($W_z/W_o/d = 6.0/15/1.5$ μm), and array B ($W_z/W_o/d = 6.0/12/1.5$ μm).

being much faster in the center than at the periphery of the optical aperture. The pronounced hole drift process from the peripheral area to the center results in the observed low-frequency roll-off. This type of roll-off is minimized in the measured E-O responses of array A due to the dilution of the photon density because of the passive waveguides between neighboring active mesas.

Fig. 13 shows the 10 Gbit/sec eye pattern measurement results for 3×3 arrays A and B and the single reference device. Here, we adopt the same optics setup as that in our E-O bandwidth measurement to collect the light output from one of the single emitters in the array. Regarding with high-speed photo-receiver module, it has been replaced with a different one (VI Systems: R50-1300;), comprised of a p-i-n photodiode and limiting amplifier with a 3-dB optical-to-electrical (O-E) bandwidth of around 30 GHz. The O-E converted signal is then fed into a sampling scope to record and analyze the eye patterns. A 10 Gbit/s non-return-to-zero (NRZ) electrical signal with a pseudo-random binary sequence (PRBS) length of 2^{15}-1 is generated through a pattern generator to drive the VCSELs. Both arrays (A and B) are tested under the optimized and same peak-to-peak driving voltage (0.9 V) to evaluate the quality of the eye patterns. Here, in the 3×3 array A (W_o: 15 μm), a bias current ($\sim$80 mA)

with a narrow convergiece is chosen (FWHM: $\sim$6°) and a moderate output power ($\sim$33 mW); refer to Table I. As can be seen, clear 10 Gbit/sec eye-opening can be achieved with both the single reference device and array A. However, for array B with SM performance (W_o: 15 μm), the measured 10 Gbit/sec eye-patterns are closed. This poor eye-opening performance can be attributed to the serious low-frequency roll-off induced by the SHB effect in the measured E-O responses, as indicated in Fig. 10, and the optical/thermal cross-talk between the different VCSEL emitters under large signal modulation in the array. The SHB effect can be minimized when the output optical spectra of the VCSEL vary from SM to MM. Here, the measured 10 Gbit/sec eye-patterns for the MM array B (W_o: 12 μm) are given for reference. We can clearly see that even for array B with the MM structure (W_o: 12 μm), the quasi-SM array A (W_o: 15 μm) can still give a much better eye-opening performance, a narrower divergence angle (6° vs. 12°), and maintain a single-spot FFP (without the indentation in the center). From a comparison of the static and dynamic measurement results for arrays A and B, as shown in Figs. 4 and 11, to those of array B with the traditional array structure, we can conclude that the proposed 3×3 array A structure can effectively narrow the divergence angle (from

12° to 6°) and significantly enhance the large signal modulation performance.

IV. Summary

We demonstrate a novel design for high-brightness, high-speed, and (quasi-) SM VCSEL array operating at the 940 nm wavelength. By using Zn-diffusion and the inclusion of oxide-relief apertures in the VCSEL units of our array, the RC-limited bandwidths can be greatly relaxed, leading to very small degradation in net E-O bandwidths of our 3 × 3 array as compared to that of the single reference device. In addition, by inserting passive waveguides to bridge the neighboring active VCSEL mesas, the coherence among different emitters in the array can be enhanced, which in turn results in a dramatic change of FFPs compared to those of the reference VCSEL array without waveguide connections. Furthermore, with the demonstrated (quasi-) SM array structure we obtain a higher WPE and much better 10 Gbit/sec eye-opening performance than for the traditional SM array with close values of W_o and W_z in each single unit of the array. This is because the SHB effect, which usually limits the static and dynamic performance of SM (high-brightness) VCSELs, can be greatly minimized due to the dilution of the photon density among the passive waveguides. In addition, interference noise among neighboring VCSEL emitters is minimized due to the increase of coherence between the VCSEL units in our proposed array structure.

Acknowledgment

References

[1] R. Safaisini, J. R. Joseph, and K. L. Lear, "Scalable high-CW-power high-speed 980-nm VCSEL arrays," *IEEE J. Quantum Electron.*, vol. 46, no. 11, pp. 1590–1596, Nov. 2010.

[2] P. Westbergh, J. S. Gustavsson, and A. Larsson, "VCSEL arrays for multicore fiber interconnects with an aggregate capacity of 240 gb/s," *IEEE Photon. Technol. Lett.*, vol. 27, no. 3, pp. 296–299, Feb. 2015.

[3] J.-L. Yen, X.-N. Chen, K.-L. Chi, J. Chen, and J.-W. Shi, "850 nm Vertical-cavity surface-emitting laser arrays with enhanced high-speed transmission performance over a standard multimode fiber," *IEEE/OSA J. Lightw. Technol.*, vol. 35, no. 15, pp. 3242–3249, Aug. 2017.

[4] N. Haghighi, P. Moser, and J. A. Lott, "Power, bandwidth, and efficiency of single VCSELs and small VCSEL arrays," *IEEE J. Sel. Topics Quantum Electron.*, vol. 25, no. 6, Nov./Dec. 2019, Art. no. 1700615.

[5] 2017. [Online]. Available: https://digitalcommons.usu.edu/smallsat/2017/all2017/122/

[6] P. Shubert, A. Cline, J. McNally, and R. Pierson, "System design of low SWaP optical terminals for free space optical communications," *Proc. SPIE*, vol. 10096, Feb. 2017, Art. no. 100960U.

[7] D. Guilhot and P. Ribes-Pleguezuelo, "Laser technology in photonic applications for space," *Instruments*, vol. 3, no. 3, Sep. 2019, Art. no. 50.

[8] R. F. Carson et al., "Surface-emitting laser technology and its application to the space radiation environment," *Proc. SPIE*, vol. 10288, Jul. 1997, Art. no. 1028806.

[9] P. M. Goorjian, "Free-space optical communication for cubesats in low lunar orbit (LLO)," *Proc. SPIE*, vol. 11272, Mar. 2020, Art. no. 1127214.

[10] J.-L. Yen, K.-L. Chi, J.-W. Jiang, Y.-J. Yang, and J.-W. Shi, "Single-mode vertical-cavity surface-emitting lasers array with Zn-diffusion aperture for high-power, single-spot, and narrow divergence angle performance," *IEEE J. Quantum Electron.*, vol. 50, no. 10, pp. 787–794, Oct. 2014.

[11] Zuhaib Khan et al., "High-brightness and high-speed vertical-cavity surface-emitting laser arrays," *Optica*, vol. 7, no. 4, pp. 267–275, Apr. 2020.

[12] R. F. Carson et al., "Progress in high-power, high-speed VCSEL arrays," *Proc. SPIE*, vol. 9766, Mar. 2016, Art. no. 97660B.

[13] A. Haglund, J. S. Gustavsson, J. Vukusic, P. Modh, and A. Larsson, "Single fundamental mode output power exceeding 6 mW from VCSELs with a shallow surface relief," *IEEE Photon. Technol. Lett.,* vol. 16, no. 2, pp. 368–370, Feb. 2004.

[14] J.-W. Shi, C.-C. Chen, Y.-S. Wu, S.-H. Guol, and Y.-J. Yang, "High-power and high-speed Zn-diffusion single fundamental-mode vertical-cavity surface-emitting lasers at 850nm wavelength," *IEEE Photon. Technol. Lett.,* vol. 20, no. 13, pp. 1121–1123, Jul. 2008.

[15] A. Furukawa, et al., "High-power single-mode vertical-cavity surface-emitting lasers with triangular holey structure," *Appl. Phys. Lett.*, vol. 85, pp. 5161–5163, Nov. 2004.

[16] N. N. Ledentsov et al., "Anti–waveguiding vertical–cavity surface–emitting laser at 850 nm: From concept to advances in high–speed data transmission," *Opt. Exp.*, vol. 26, pp. 445–453, Jan. 2018.

[17] J.-W. Shi et al., "Single-mode, high-speed, and high-power vertical-cavity surface-emitting lasers at 850 nm for short to medium reach (2 km) optical interconnects," *IEEE/OSA J. Lightw. Technol.,* vol. 31, no. 24, pp. 4037–4044, Dec. 2013.

[18] A. Haglund, J. S. Gustavsson, P. Modh, and A. Larsson, "Dynamic mode stability analysis of surface relief VCSELs under strong RF modulation," *IEEE Photon. Technol. Lett.,* vol. 17, no. 8, pp. 1602–1604, Aug. 2005.

[19] J.-W. Shi, J.-C. Yan, J.-M. Wun, J. (J.) Chen, and Y.-J. Yang, "Oxide-relief and Zn-diffusion 850 nm vertical-cavity surface-emitting lasers with extremely low energy-to-data-rate ratios for 40 Gbit/sec operations," *IEEE J. Sel. Topics Quantum Electron.,* vol. 19, no. 2, Mar./Apr. 2013, Art. no. 7900208.

[20] C.-L. Cheng, N. Ledentsov, Z. Khan, J.-L. Yen, N. N. Ledentsov, and J.-W. Shi, "Ultrafast Zn-diffusion and oxide-relief 940 nm vertical-cavity surface-emitting lasers under high-temperature operation," *IEEE J. Sel. Topics Quantum Electron.,* vol. 25, no. 6, Nov./Dec. 2019, Art. no. 1700507.

[21] F. Koyama and X. Gu, "Beam steering, beam shaping, and intensity modulation based on VCSEL photonics," *IEEE J. Sel. Topics Quantum Electron.*, vol. 19, no. 4, pp. 1701510–1701510, Jul./Aug. 2013.

[22] K.-L. Chi et al., "Strong wavelength detuning of 850 nm vertical-cavity surface-emitting lasers for high-speed (>40 Gbit/sec) and low-energy consumption operation," *IEEE J. Sel. Topics Quantum Electron.,* vol. 21, no. 6, Nov./Dec. 2015, Art. no. 1701510.

[23] M. E. Warren et al., "On-axis far-field emission from two-dimensional phase-locked vertical cavity surface-emitting laser arrays with an integrated phase-corrector," *Appl. Phys. Lett.,* vol. 61, pp. 1484–1486, Sep. 1992.

[24] M. Orenstein, E. Kapon, J. P. Harbison, L. T. Florez, and N. G. Stoffel, "Large two-dimensional arrays of phase-locked vertical cavity surface emitting lasers," *Appl. Phys. Lett.*, vol. 60, pp. 1535–1537, Mar. 1992.

Jie-Chen Shih was born in Pingtung, Taiwan, on October 7, 1995. He graduated from the Department of Electrical Engineering, Tunghai University, Taichung City, Taiwan. He is currently working toward the master's degree with the Department of Electrical Engineering, National Central University, Taoyuan, Taiwan. His current research interests include high-speed and high-power VCSELs.

Zuhaib Khan was born in Uttar Pradesh, India, in 1992. He graduated from the Department of Electronics and Communication Engineering, Jamia Millia Islamia, New Delhi, India. He is currently working toward the Ph.D. degree from the Department of Electrical Engineering, National Central University, Taoyuan, Taiwan. His current research interests include high-speed, high power VCSELs for application to optical interconnects, 3D-sensing, autonomous LIDAR, and time of flight technology.

Yung-Hao Chang was born in Tainan, Taiwan, on November 5, 1996. He graduated from the Department of Electrical Engineering, Yuan Ze University, Taoyuan City, Taiwan. He is currently working toward the master's degree with the Department of Electrical Engineering, National Central University, Taoyuan, Taiwan. His current research interests include high-speed and high-power VCSELs.

Jin-Wei Shi (Senior Member, IEEE) was born in Kaohsiung, Taiwan, on January 22, 1976. He received the B.S. degree in electrical engineering from National Taiwan University, Taipei, Taiwan, in 1998 and the Ph.D. degree from the Graduate Institute of Electro-Optical Engineering, National Taiwan University, in 2002. In 2000 and 2001, he was a Visiting Scholar with the University of California, Santa Barbara (UCSB), CA, USA. During 2002–2003, he was a Postdoc with Electronic Research and Service Organization, Industrial Technology Research Institute. In 2003, he joined the Department of Electrical Engineering, National Central University, Taoyuan, Taiwan, where he is currently a Professor. In 2011, he again joined the ECE Department of UCSB as a Visiting Scholar. He has authored or coauthored more than 140 Journal papers, 160 conference papers, and holds 20 patents. His current research interests include ultra-high speed/power optoelectronic devices, such as photodetectors, electro-absorption modulators, sub-millimeter wave photonic transmitters, and semiconductor lasers. He was an Invited Speaker at the 2002 IEEE LEOS, 2005 SPIE Optics East, 2007 Asia-Pacific Microwave Photonic conference (AP-MWP), 2008 Asia Optical Fiber Communication & Optoelectronic Exposition & Conference, 2011 Optical Fiber Communication (OFC), and 2012 IEEE Photonic Conference. He was on the Technical Program Committees for the OFC 2009-2011, 2012 SSDM, 2012 MWP, and 2013 Asia-Pacific CLEO. In 2007, he was the recipient of the Excellent Young Researcher Award from the Association of Chinese IEEE and in 2010, the Da-You Wu Memorial Award.